PHYSICAL REVIEW A **97**, 023414 (2018)

Tracking the ultrafast XUV optical properties of x-ray free-electron-laser heated matter with high-order harmonics

Gareth O. Williams,[1,*] S. Künzel,[1] S. Daboussi,[2] B. Iwan,[3] A. I. Gonzalez,[3] W. Boutu,[3] V. Hilbert,[4] U. Zastrau,[5] H. J. Lee,[6] B. Nagler,[6] E. Granados,[6] E. Galtier,[6] P. Heimann,[6] B. Barbrel,[7] G. Dovillaire,[8] R. W. Lee,[9] J. Dunn,[9] V. Recoules,[10] C. Blancard,[10] P. Renaudin,[10] A. G. de la Varga,[11] P. Velarde,[11] P. Audebert,[12] H. Merdji,[3] Ph. Zeitoun,[2] and M. Fajardo[1]

[1]*GoLP/Instituto de Plasmas e Fusão Nuclear-Laboratório Associado, Instituto Superior Técnico, Universidade de Lisboa, 1049-001 Lisboa, Portugal*
[2]*Laboratoire d'Optique Appliquée, ENSTA ParisTech, CNRS, École Polytechnique, UMR 7639, Chemin de la Hunière, 91762 Palaiseau, France*
[3]*LIDYL, CEA, CNRS, Université Paris-Saclay, CEA Saclay, 91191 Gif-sur-Yvette, France*
[4]*Institute of Optics and Quantum Electronics, Friedrich-Schiller University Jena, Max-Wien-Platz 1, 07743 Jena, Germany*
[5]*European XFEL, Holzkoppel 4, 22869 Schenefeld, Germany*
[6]*SLAC National Accelerator Laboratory, 2575 Sand Hill Road, Menlo Park, California 94025, USA*
[7]*Lawrence Berkeley National Laboratory, 1 Cyclotron Road, Berkeley, California 94720, USA*
[8]*Imagine Optic, 18 Rue Charles de Gaulle, 91400 Orsay, France*
[9]*Lawrence Livermore National Laboratory, Livermore, California 94550, USA*
[10]*CEA-DAM-DIF, Bruyères Le Châtel, 91297 Arpajon Cedex, France*
[11]*Instituto de Fusión Nuclear, Universidad Politécnica de Madrid, José Gutiérrez Abascal 2, 28006 Madrid, Spain*
[12]*LULI, École Polytechnique, CNRS, CEA, UPMC, route de Saclay, 91128 Palaiseau, France*

(Received 29 May 2017; revised manuscript received 17 January 2018; published 14 February 2018)

We present measurements of photon absorption by free electrons as a solid is transformed to plasma. A femtosecond x-ray free-electron laser is used to heat a solid, which separates the electron and ion heating time scales. The changes in absorption are measured with an independent probe pulse created through high-order-harmonic generation. We find an increase in electron temperature to have a relatively small impact on absorption, contrary to several predictions, whereas ion heating increases absorption. We compare the data to current theoretical and numerical approaches and find that a smoother electronic structure yields a better fit to the data, suggestive of a temperature-dependent electronic structure in warm dense matter.

DOI: 10.1103/PhysRevA.97.023414

I. INTRODUCTION

Currently, one of the most challenging areas in plasma physics is where the condensed matter and classical plasma descriptions begin to fail, referred to as warm dense matter (WDM) [1]. In this state, electrons are coupled through their Coulomb and quantum interactions in the presence of a positive-ion background field and constitute an archetypal many-body quantum system [2]. In WDM the kinetic energy of the electrons is of the order of the potential energy of the surrounding ions, and the electron temperature is of the order of the Fermi temperature. Difficulties in modeling arise from the lack of basic simplifying assumptions that can be made, and a full quantum description of many electrons in a given ion configuration is required. As classical plasma treatments fail, numerical methods typically used for the description of condensed matter such as density functional theory (DFT) are applied, yet are complicated by finite temperatures and computational demands [1,3]. Difficulty in general theoretical treatments restricts our predictive capabilities of key physical parameters such as conductivity and equation of state, making experimental data acquisition of paramount importance.

Measuring radiation transport in WDM tests our basic understanding of the electronic structure of these plasmas, provides practical information through opacity tables, and benchmarks codes that are routinely used to predict the radiative transfer properties of solids, astrophysical objects, and man-made plasmas [4]. Visible probes are capable of measuring low-energy (a few eV) transitions around the occupied states where typical absorption lengths are on the order of nanometers [5–7]. Yet the higher-energy electronic structure above the plasma frequency, ω_p, dictates the radiative transport properties in WDM as absorption lengths are typically a hundred times that of optical light. Above ω_p, free-free optical transitions are the dominant absorption pathway in the absence of bound transitions. These free-free transitions are solely responsible for the opacity of the warm dense deuterium-tritium layer in inertial confinement fusion (ICF) implosions, which governs the radiation transport and hence critical to predict the level of preheating of the fuel during the compression phase [8]. It has been shown that detailed quantum molecular dynamics (QMD) calculations of the opacity can differ from tabulated values by as much as a factor of 2 in the strongly degenerate regime, highlighting the need for direct comparisons between

---

[*] gareth.williams@ist.utl.pt

2469-9926/2018/97(2)/023414(9)

experiment and theory [8]. The initial and final electron states that determine the optical transition probability are shaped by both the electronic and crystal (ionic) structure. The individual role of each in the free-free absorption process in WDM is not clearly understood. For example, some theories predict an increase in absorption with T_e due to an increased number of final states, and a negligible role of T_i [9]. Other theories predict that a smearing of electron occupations caused by T_e can increase absorption to varying degrees depending on the assumptions used, and T_i can play a significant role due to the loss of crystal structure [10]. The role of T_e and T_i in the absorption process has never been experimentally determined at these photon energies, due to the picosecond time scale temperature coupling of the electrons and ions. Here, we use an ultrafast heating and probe pulse to elucidate the role of T_e and T_i. By separating the electron and ion heating time scales, and measuring the time-resolved absorption, we can infer the role of purely electronic excitations (due to an increase in the electron temperature, T_e) and structural changes (due to an increase in the ion temperature, T_i) in radiation transport that is currently unresolved [9–11].

In this article, we present data of free-free XUV absorption in solid-density aluminum and show that by separating the electron and ion heating in time we can identify how they affect radiation transport in WDM. We show that an increase in T_i causes an increase in photon absorption due to crystal decomposition. The influence of T_e is shown to be relatively small, contrary to several predictions, including calculations conducted in this study [9,10]. The results show that the higher-energy transitions (made available with increased T_e) have a smaller absorption cross-section than commonly predicted, and smoothing of the electronic structure with increased T_e reduces this dependence. We use what is generally considered to be one of the most accurate treatments of the optical properties of warm dense matter, DFT, to show that the predicted sharp increase in absorption with T_e is due to the larger transition probabilities of higher-energy optical transitions. As this dependence is not observed experimentally here, we conclude a temperature dependence of the electronic structure smoothes this sharp increase in absorption probability.

II. EXPERIMENTAL SETUP

There are two main experimental challenges: First, to reliably measure changes in absorption requires probing significant (more than one absorption length, >400 nm) thicknesses of material with a uniform energy density. Second, to separate the effect of T_e and T_i in time requires a source that can deposit sufficient heating energy on a femtosecond time scale, and a separate XUV probe pulse of similar duration to measure the absorption. X-ray free-electron lasers (XFELs) can provide ideal heating pulses for WDM and have demonstrated uniform heating of micrometer-thick foils, allowing the creation of volumes of plasma with a well-defined energy density on a femtosecond time scale [12–14]. Gradients do exist, however, in the temporal domain of the T_e and T_i, and in the direction transverse to the XFEL pulse direction. High-order-harmonic generation (HHG) using an infrared (IR) laser was used as a probe pulse as it is a flexible ultrafast source yielding photon energies in the required XUV range. Using these two sources in a pump-probe arrangement decouples the ultrafast XFEL heating and XUV probing, allowing the XUV absorption due to ultrafast heating of the electrons (femtosecond time scale) and ions (picosecond time scale) to be tracked in time.

The spectral region dominated by free-free absorption in aluminum is above ω_p, (~15 eV), and below the first photoionization edge (~72 eV) at temperatures below any significant collisional ionization ($T_e < 15$ eV). This makes aluminum an ideal material for reconciling the role of T_e and T_i in the free-free photoabsorption process. Previous measurements of warm dense aluminum have been made at $T_e = T_i = 1$ eV, showing little change from cold [11], in agreement with [9] yet contrary to [10]. Extending our knowledge in this regime requires higher temperatures and the separation of T_e and T_i, which has not yet been studied.

A solid aluminum foil target of 600 nm in thickness was heated with a 35-fs XFEL pulse of 3 keV photons, resulting in <1% of the atoms in the central spot being directly photoionized, producing electrons with energies of ~1.5 keV. When the XFEL pulse ends, high-energy electrons are no longer generated and a thermal electron distribution is expected to form within ~100 fs [15,16], after which the much heavier ions thermalize with the electrons on a picosecond time scale.

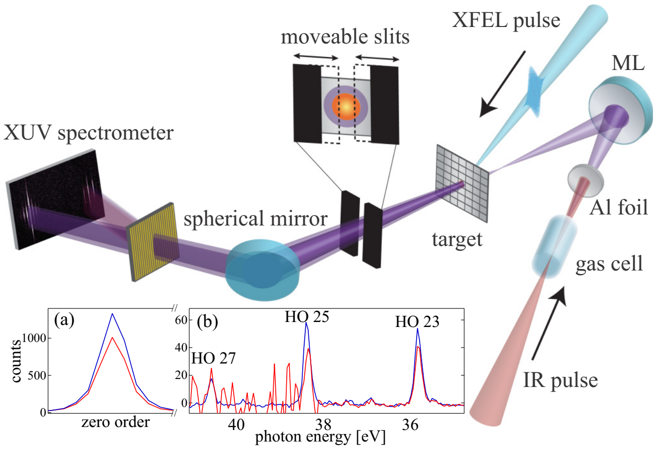

FIG. 1. The experimental arrangement for the measurement of XUV absorption in an XFEL heated aluminum foil. A 40 fs IR pulse at a wavelength of 800 nm and intensity ~10^{15} W cm^{-2} is focused into a gas cell of 1.5 cm in length and filled with argon (Ar) at a pressure of 30 mbar to generate high-order harmonics in the XUV. The XUV beam is then focused by a multilayer mirror (ML) near the target plane. The XUV pulse is partially transmitted through the foil, and the remaining XUV light is absorbed. An adjustable slit is placed after the target to block the XUV light that does not pass through the plasma. The absorption of three high-order harmonics through the foil target is measured using an XUV spectrometer. A typical spectrum transmitted through the cold (blue) and heated (noisy red) aluminum foil is shown in the inset. By dividing the red by the blue, we can extract the transmission relative to cold at three photon energies. Spectra transmitted through the foil were measured at different times with respect to the peak of the XFEL. The measured relative transmission time histories are plotted in Figs. 4 and 5. The (a) zero order and (b) spectrally resolved regions are separated for clarity in the inset. The noise in the plasma shot in (b) is due to scattered hard x rays. The harmonic order (HO) of the three photon energies is shown in (b).

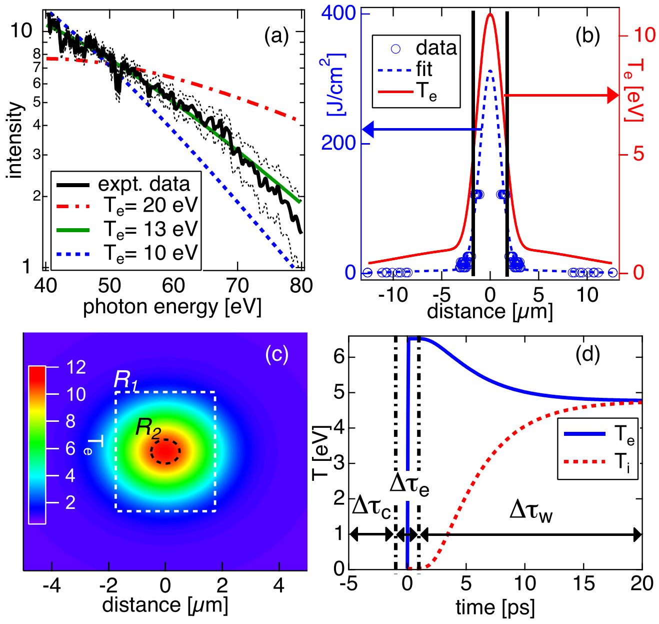

FIG. 2. (a) The smoothed time-integrated XUV plasma emission measurement (solid noisy thick black line) with error bars (dashed thin black lines), and the best fit with a peak electron temperature of $T_e = 13 \pm 3.25$ eV (solid green line). (b) The measured fluence profile of the XFEL spot on target (blue circles) and fit (dashed blue line) which is used in the TTM to calculate the temperature profile across the target (solid red line, a 0.5-μm-width line out). The solid black lines indicate the borders of the probed region R_1 in (c). (c) The calculated two-dimensional peak electron temperature profile using the measured beam fluence profile. The dashed lines in (c) enclose the area probed by the XUV pulse, R_1, and the area that dominates the XUV emission spectrum, R_2, in (a). (d) The calculated spatial average of the electron (solid blue line) and ion (dashed red line) temperatures in time of the probed area, R_1, from the TTM. The three time scales of interest are shown in (d) (arrows and dash-dotted lines): $\Delta\tau_c$ is the cold solid foil, $\Delta\tau_e$ is the time scale of electron heating only, and $\Delta\tau_w$ is the time scale of electron-ion coupling.

The HHG probe pulse spectrum contains three distinct photon energies (35.7, 38.8, and 41.8 eV) in a <40 fs pulse duration (Fig. 1). The absorption of the XUV probe is measured in transmission relative to the unperturbed foil at a range of time delays after the peak of the XFEL pulse (Fig. 1 inset). Each transmission measurement consists of ten accumulated shots, and the temporal resolution was 1 ps due to timing drifts between the two pulses. An example of a typical transmission spectrum of the cold and heated foil are shown in Fig. 1 (inset). The target conditions as a result of XFEL heating are discussed in Sec. III.

III. TARGET HEATING

The time history (or evolution) of the target conditions was determined using a combination of experimental data and modeling which is shown in Fig. 2. The peak T_e of the plasma, which corresponds to the hottest electron temperature achieved in space and time, was measured using a time-integrated XUV emission spectrometer giving a best fit to a temperature of $T_e = 13 \pm 3.25$ eV [Fig. 2(a)]. To estimate the range of temperatures in the XFEL spot, the spatial fluence profile of the XFEL pump was measured [Fig. 2(b), circles] and the measured fluences were then used in combination with tabulated heat capacities to calculate the peak electron temperatures of the target in one dimension [Fig. 2(b), solid red line] [17]. The calculated peak electron temperature of $T_e = 12.6 \pm 3.15$ eV in Fig. 2(b) is in good agreement with the measured peak value from plasma emission of $T_e = 13 \pm 3.25$ eV [Fig. 2(a)]. Due to the experimental geometry, the probe beam samples a range of temperatures in time and space within the XFEL spot which cannot be reliably deconvolved. The spatial distribution of the peak electron temperature from the two-temperature model (TTM, discussed below) is shown in Fig. 2(c), and the area sampled by the probe pulse is shown as R_1. Region R_1 corresponds to a range of values of T_e and T_i in time, and the average T_e and T_i within this region are shown in Fig. 2(d), illustrating the separation of T_e and T_i in time. The three temporal regions of interest are shown in Fig. 2(d) (arrows) and explained in the caption. As there exist uncertainties in the measured fluence profiles, heat capacities, and inferred temperatures from emission spectra, the exact temperatures calculated with the TTM cannot be considered absolute. As such we have estimated an error of 25% for all calculated temperatures to encapsulate these errors. The details of the TTM are now discussed.

We apply a method used to describe T_e and T_i in time, which is commonly applied to ultrafast laser heating of solids, the TTM. The coupled equations are given by

$$\begin{aligned} C_e(T_e)\frac{dT_e}{dt} &= G_{ep}(T_i - T_e) + S(t), \\ C_i(T_i)\frac{dT_i}{dt} &= G_{ep}(T_e - T_i), \end{aligned} \tag{1}$$

where $C_e(T_e)$ and $C_i(T_i)$ are the temperature-dependent electron and ion heat capacities, T_e and T_i are the electron and ion temperatures, G_{ep} is the electron-ion coupling term, and $S(t)$ is the source term which represents the deposition of the laser energy in time [18].

The fraction of energy of the XFEL pulse absorbed in the foil is estimated from tabulated values of cold solid absorption coefficients [19]. The absorbed energy governs how the electron temperature increases due to the time-dependent laser energy flux term, $S(t)$ in Eqs. (1), which has a Gaussian temporal profile (FWHM = 35 fs).

The electron and ion heat capacities, $C_e(T_e)$ and $C_i(T_i)$, depend directly on the equation of state (EOS) of aluminum, for which experimental data spanning large temperature ranges (up to tens of eVs) at solid density are scarce, and many models exist. We attribute a temperature to the electron and ion system through temperature-dependent heat capacities of aluminum from the SESAME EOS tables, as they cover a broad range of temperatures and contain a separate EOS for the electrons and ions, which are in broad agreement with other models (SESAME material number 3720) [17]. Early-time-scale phenomena that may result in nonthermal electron distributions, such as photoionization, autoionization, collisional ionization, and their corresponding inverse processes cannot be treated within the TTM, and the approximation of instant electron thermalization is used. Although relaxation is complex, all the electronic paths have femtosecond relaxation time scales and recent studies have shown that this approximation is appropriate for the case of solid-density metallic systems [16,20].

The energy coupling of the electrons and ions is governed by the coupling coefficient, G_{ep}, in Eqs. (1). A survey of the literature presents values in the range of $G_{ep} \approx (0.5\text{–}4) \times 10^{17}$ W m^{-3} K^{-1} (as shown in Fig. 3) and depends on many factors such as the electronic structure and temperature [21,27], phonon modes [28], and the energy density in the material [29]. Even using the lowest reported values of G_{ep}, the TTM predicts melting times of ∼200 fs for the heating conditions in this study, which is unphysically fast for aluminum and not within the accepted ranges reported elsewhere. Various studies report melting times of aluminum within the range of 1.5 to 3.5 ps [23,28,30–34]. To ensure the melting time scales are in agreement with the accepted values, we must use a time-dependent G_{ep}.

Temperatures achieved in this study are typically higher than reported elsewhere, which further complicates the choice of G_{ep} [21,23]. The highest tabulated value for G_{ep} is taken from a theoretical study by Lin *et al.* [21] for an electron temperature of $T_e = 5$ eV at solid density and this is taken as the upper limit. Several values of G_{ep} from other studies are shown in Fig. 3 along with several functions that ensure the ions reach the melting temperature of aluminum at ∼1.5 ps, to agree broadly with other studies of ultrafast melting of aluminum [23,28,30–34]. The choice of the function describing G_{ep} in time has two basic boundary conditions: (1) the melting temperature of the ions must be reached at approximately the time at which melting has been shown to occur in similar studies and (2) the values of G_{ep} must lie within values reported in other studies. Using these boundary conditions, various functions can be used to describe G_{ep} in time, yet the exact form does not significantly affect the calculated transmission curves. We use the function $G_{ep} = G_{\max} \exp[-(2\text{ ps}/t)^2]$ to describe the electron-ion energy coupling in time, where $G_{\max} = 3.47 \times 10^{17}$ W m^{-3} K^{-1} is the maximum value of G_{ep} found in the literature from [21], t is time, and the exponential function with a delay time of 2 ps ensures the melting temperature is reached within ∼1.5 ps after the pulse peak (short-dashed black line in Fig. 3).

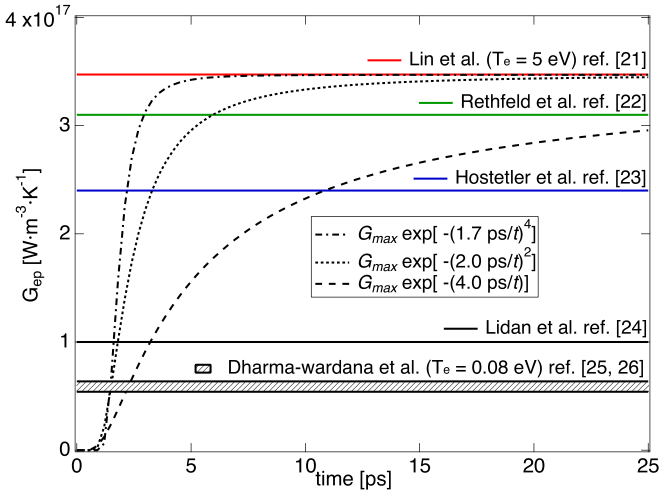

FIG. 3. The electron-phonon coupling coefficient used in the TTM, G_{ep}, as a function of time from the peak of the heating pulse for three functions that give a melting time of ∼1.5 ps, where the maximum value of G_{ep} is given as $G_{\max} = 3.47 \times 10^{17}$ W m^{-3} K^{-1} (broken black lines): the theoretical value of G_{ep} at an electron temperature of 5 eV (red line) [21], theoretical value of G_{ep} (green line) [22], experimental value of G_{ep} (blue line) [23], experimental value of G_{ep} (solid black line) [24], theoretical values of the coupled mode calculation in the range of T_e in this study and $T_i = 0.08$ eV (shaded black region) [25,26].

From the combined data and modeling in this section, we conclude that although heating solids with an XFEL involves complex pathways on the femtosecond time scale, we can infer that a thermalized electron distribution is achieved within 100 fs of the XFEL pulse and ion heating occurs on the picosecond time scale, leaving a window of several picoseconds to observe the effect of electron and ion heating separately. The time-resolved transmission data are discussed in Sec. IV.

IV. TRANSMISSION RESULTS

The zero-order (integrated spectrum) transmission measurements provide a global trend of the data and are shown in Fig. 4 along with several predictions from theory. The spectrally resolved data give valuable information on the dynamics, as the absorption is quite sensitive to the three photon energies used in this study and is shown in Fig. 5. The cold solid absorption was measured without the spectrometer and

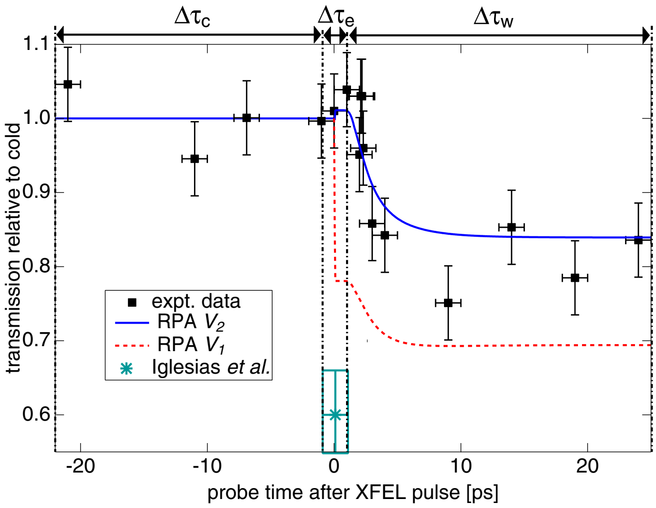

FIG. 4. The experimental transmission of zero order (all harmonics) relative to cold of a 600 nm aluminum foil heated by an XFEL pulse (black squares). The time axis is relative to the peak of the XFEL pulse. Calculated transmission values for the electron-ion potential V_1 (dashed red line) and V_2 (solid blue line), for the average transmission of the probed region, are shown. A delay in electron-ion coupling is incorporated into the TTM to give a heating rate in agreement with other studies (detailed in Sec. III). A semianalytic model by Iglesias *et al.* [9] predicting changes due to electron heating is shown in the $\Delta\tau_e$ phase (boxed green star). The three time scales of interest are shown (arrows and dash-dotted lines): $\Delta\tau_c$ is the cold solid foil, $\Delta\tau_e$ is the time scale of electron heating only, and $\Delta\tau_w$ is the time scale of electron-ion coupling.

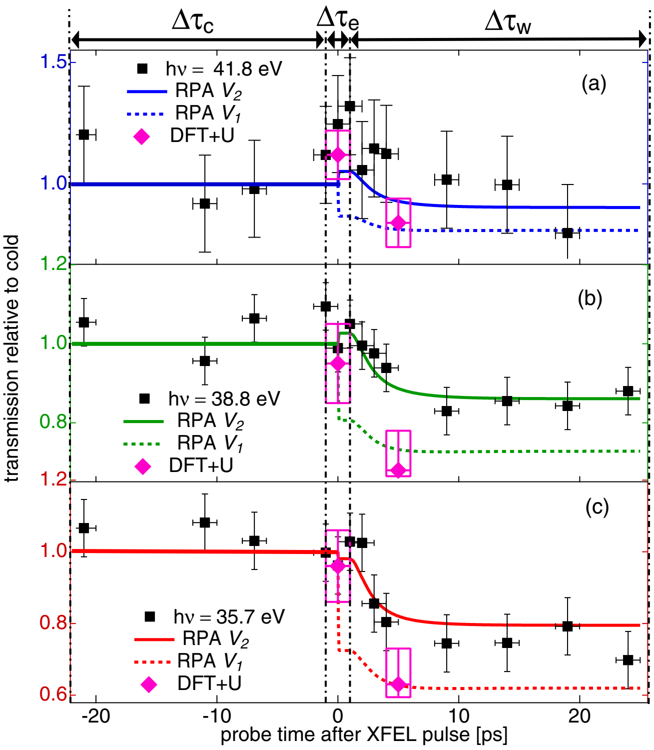

FIG. 5. Spectrally resolved relative transmission through the XFEL heated foil for the three photon energies of (a) 41.8 eV, (b) 38.8 eV, and (c) 35.7 eV used in this study. The calculated relative transmission for the temperatures in the probed region [R_1 in Fig. 2(c)] for the electron-ion potentials V_1 (dashed line) and V_2 (solid line) is shown for each photon energy. The three time scales of interest are shown (arrows and dash-dotted lines): $\Delta\tau_c$ is the cold solid foil, $\Delta\tau_e$ is the time scale of electron heating only, and $\Delta\tau_w$ is the the time scale of electron-ion coupling. The results of DFT+U calculations are shown for the $\Delta\tau_e$ and $\Delta\tau_w$ time scales of interest and discussed in Sec. VI.

hence yielded the weighted average transmission of the entire spectrum, giving an absorption coefficient of $\alpha_c^{\mathrm{ex}} = 2.5 \times 10^6$ m^{-1} when corrected for an oxide layer of 10 nm which is in reasonable agreement with values reported elsewhere ($\alpha_c^{cxro} = 2.3 \times 10^6$ m^{-1}) [35]. Two features are clearly noticeable from the data in Figs. 4 and 5: first, there is no significant change in transmission during the electron heating time scale, $\Delta\tau_e$, and second, there is a steady decrease in transmission up to ~10 ps in the ion heating phase, $\Delta\tau_w$. Other studies have observed a slight decrease, followed by an increase in transmission as a function of increasing fluence (and hence temperature) in the $\Delta\tau_e$ phase [36]. This behavior was attributed to nonlinear absorption processes present in [36] due to the high pulse intensity. As nonlinear effects caused by the probe beam are assumed to be absent in the present study (the pulse intensity is 10^{-5} times lower here), it makes a direct comparison of the two data sets impossible.

The spectrally resolved data in Fig. 5 show a similar temporal dependence (decrease in transmission during the $\Delta\tau_w$ phase) when compared with zero-order data in Fig. 4. The decrease in transmission is greater for lower photon energies, which is generally expected in free-free absorption. Only minor changes occur at a photon energy of 41.8 eV in Fig. 5(a) (although the data are noisy); for 38.8 eV the transmission saturates at about 85% [Fig. 5(b)], and for 35.7 eV the transmission saturates at about 75% [Fig. 5(c)]. The observed changes in transmission stagnate after a delay of 10 ps, which corresponds to the stagnation of the increasing ion temperature [shown in Fig. 2(d)]. The time scale of the observed changes is consistent with an absorption mechanism dominated by the disintegration of the crystal structure caused by increasing T_i.

We compare the data with theories that can treat the linear optical response of a temperature-dependent electronic and ion structure. Two approaches are used: a semianalytical model for initial comparison which incorporates the commonly used random phase approximation (RPA) [10] in Sec. V, and numerical DFT for more precise calculations in Sec, VI.

V. THEORETICAL MODEL

An appropriate theoretical model must be able to account for changes to the optical properties caused by electron and ion heating separately, in the solid-to-plasma transition. We follow the approach originally proposed by Ron and Tzoar to calculate the dielectric function of quantum plasmas [37] and later applied to the specific case of warm dense aluminum by Vinko *et al.* [10]. To account for collisions when the light frequency, ω, is greater than the plasma frequency ω_p, the dielectric function assumes the form $\epsilon(\omega) = 1 - \frac{\omega_p^2}{\omega^2} + \epsilon'(\omega)$, where

$$\epsilon'(\omega) = A \int q^6 \frac{V(q)^2}{|\epsilon_e(q,\omega)|^2} S_{ii}(q)[\epsilon_e(q,\omega) - \epsilon_e(q,0)]dq, \quad (2)$$

$A = \frac{1}{6\pi^2}\frac{n_i}{m_e^2\omega^4}$, n_i is the ion density, m_e the electron mass, $V(q)$ is the electron-ion pseudopotential in momentum space, S_{ii} is the static ion-ion structure factor, $\epsilon_e(q,\omega)$ is the electron dielectric function, and q is the scattered momentum. Following [10], we use a form of $V(q)$ for the potential defined in space, r, as $V_1(r) = -\frac{Ze^2}{4\pi\epsilon_0 r}$ for $r > r_c$ and $V_1(r) = 0$ for $r < r_c$ with $r_c = 60.8$ pm, where r is the radial distance from the nucleus. A cartoon of the physical interpretation of the cutoff radius is shown in Figs. 6(a) and 6(b) and the form of $V_1(r)$ is shown as a sharp red line in Fig. 6(c). Using Eq. (2) the absorption coefficient, $\alpha = \frac{2\omega}{c}\mathrm{Im}\sqrt{\epsilon(\omega)}$, is calculated for a range of electron and ion temperatures in space and time (detailed in

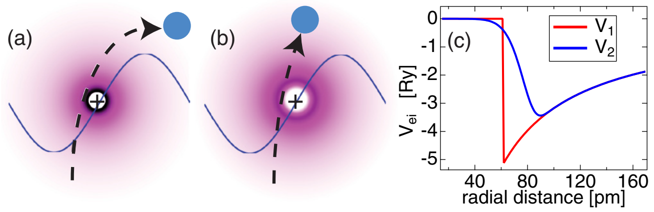

FIG. 6. An electron absorbing energy from an optical field in the presence of an ion represented by a pseudopotential of the nucleus and bound electrons with (a) small and (b) large cutoff radius. Shielding of the nucleus by the bound electrons is represented by the cutoff radius, r_c, which determines the range of potentials the electron can interact with. (c) The pseudopotential approach to treating the electron-ion potential near the bound (core) electrons, for a sharp cutoff radius V_1 (sharp red curve) and a soft cutoff V_2 (smooth blue curve) according to Eq. (3).

Sec. III) to give the time-dependent transmission of the probe beam. The same result in Eq. (2) was derived by Hopfield *et al.* to describe photoemission from solids and was shown to be accurate to order $V(q)^2$ in the regime of a linear current response to an electric field [38]. The electron dielectric function, $\epsilon_e(q,\omega)$, is treated in the RPA for a homogeneous electron gas, which ignores microscopic electron-electron interactions. Partially analytic solutions are used for $\epsilon_e(q,\omega)$ as detailed in [39]. The static ion-ion structure factor, S_{ii}, is calculated using the semianalytical approach given by [40], which has shown to be a good match with DFT calculations [10]. The pseudopotentials used in this study assume radial symmetry and ignore bound electron excitations which are assumed to occur only within the first 100 fs and do not significantly affect the data.

The cold solid absorption coefficient in the $\Delta\tau_c$ phase calculated using Eq. (2), $\alpha_c^{V_1} = 1.8 \times 10^6\ \mathrm{m}^{-1}$, is somewhat underestimated compared to the experimental cold solid value measure here ($\alpha_c^{\mathrm{ex}} = 2.5 \times 10^6\ \mathrm{m}^{-1}$). This has been observed elsewhere when compared to other tabulated values [10]. Changes in transmission due to electron heating in the $\Delta\tau_e$ phase are clearly overestimated when compared to the data (dashed line, V_1, in Fig. 4). Other studies predict a similar trend (reduced transmission with increasing T_e) due to reduced screening of the electron-ion potential and a decrease in degeneracy, freeing up final states (green star in Fig. 4) [9]. A further decrease in transmission is then predicted due to ion heating in the $\Delta\tau_w$ phase in Fig. 4 (dashed line), which is compounded by the initial change due to electron heating and overestimates the drop in transmission and is not a good fit to the data.

The model used in this study has essentially three terms that govern the absorption, S_{ii}, $\epsilon_e(q,\omega)$, and $V(q)$. The static ion structure factor $S_{ii}(q)$ is a well-studied property of liquids and plasmas and shown to be well modeled by DFT [41]. We use an analytic form that matches well with DFT [10,40] and do not consider it to be a large source of error in our theoretical predictions. The electron response is governed by $\epsilon_e(q,\omega)$ and is treated in the RPA, which neglects electron correlation effects yet has shown to be a good approximation in the temperature and density ranges in this study [42]. The electron-ion potential, $V(q)$, represents the nucleus and bound electrons together in an effective potential. The exact form of the electron-ion pseudopotential, $V(q)$, has a large impact on the optical properties and has been a source of debate in the literature [43,44].

To explore the role of this potential in predicting the changes in transmission, we now consider other possible forms of $V(q)$. It was reported by Gericke *et al.* that the sharp cutoff near the core of the electron-ion potential can be unphysical, and a smoother potential is more consistent with recent experiments [45]. We incorporate smoothing through a factor, β, to mitigate an unphysically sharp cutoff and strong oscillations when the potential is transformed to momentum space, given by

$$V_2(r) = -\frac{Ze^2}{4\pi\epsilon_0 r}\left[1 - \exp\left(-\frac{r^\beta}{r_c^\beta}\right)\right], \tag{3}$$

where Z is the ionization degree ($Z \approx 3$ for $T_e < 13$ eV), e is the electron charge, and ϵ_0 is the vacuum permittivity and is shown in Fig. 6(c) (smooth blue line) [45]. Using $V_2(r)$ with values of $r_c = 79$ pm and a smoothing factor of $\beta = 10$, a good fit with the data is found over the temperature range (Figs. 4 and 5). We note that other combinations of r_c and β can yield similar results that lie within the error bars of the data, yet overall are in the ranges $r_c = 79 \pm 5$ and $\beta = 2$–10. A better agreement with the cold solid absorption coefficient calculated with the smoothed potential ($\alpha_c^{V_2} = 2.6 \times 10^6\ \mathrm{m}^{-1}$) and the experimental value from this study ($\alpha_c^{\mathrm{ex}} = 2.5 \times 10^6\ \mathrm{m}^{-1}$) is also found.

Using the absorption model proposed by Vinko *et al.* with a smoothed potential V_2 yields a better fit to the data compared to a sharp cutoff potential V_1, as shown in Figs. 4 and 5 [10]. Although we note good agreement between the theoretical model and our data when the pseudopotential V_2 is used, we cannot infer that this potential is accurate or suitable for application elsewhere. The calculated absorption depends on other approximations such as the RPA, which assumes a noninteracting electron gas. More sophisticated (self-consistent) treatments of the electron system may improve results when used in combination with other treatments of $V(q)$. Hence, modifications to both the $V(q)$ and $\epsilon_e(q,\omega)$ may be necessary, yet their exact individual forms and temperature dependence cannot be discerned from the data. Nevertheless, we have shown that by using a more physical, smoothed $V_2(q)$, a much improved fit to the data is achieved over all time scales, which represents an improvement to the model when applied to nonequilibrium warm dense aluminum.

VI. DFT SIMULATIONS

For a more accurate treatment of the optical properties, some of the assumptions used in the model in Sec. V must be reexamined, namely, (1) a homogeneous free electron gas, (2) spherical symmetry, and (3) a self-consistent electronic and ion structure. DFT is a more accurate and widely used calculation method that can overcome these assumptions to calculate the optical properties of a self-consistent electronic and ion structure in three dimensions [7,46–48]. The DFT calculations were performed using the VASP package [46,49,50]. A plane-wave basis set and the projector augmented wave (PAW) methods were used in conjunction with the generalized gradient approximation of Perdew, Burke, and Ernzerhof [51]. A pseudopotential including 11 electrons was used. For the calculations in which a frozen crystal lattice is assumed, we use a single atom with infinite fcc symmetry and a fine ($20 \times 20 \times 20$) k-point mesh in the Monkhorst-Pack scheme [52]. The calculations in which the ions are mobile (above melting temperature) are conducted using four atoms in an $8 \times 8 \times 8$ k-point mesh. The number of bands used was sufficient to include enough free states for the optical properties to be calculated in the region of interest. The ions are allowed to move over several hundreds of femtoseconds, after which the optical properties are calculated with the current ion positions [53]. The optical properties are averaged over three directions in the unit cell. The system is then restarted from the previous position and the procedure is repeated. An average of 22 runs was used for the $T_i = 2$ eV calculation, spanning about 10 ps, and the electron temperature was fixed at $T_e = 6$ eV.

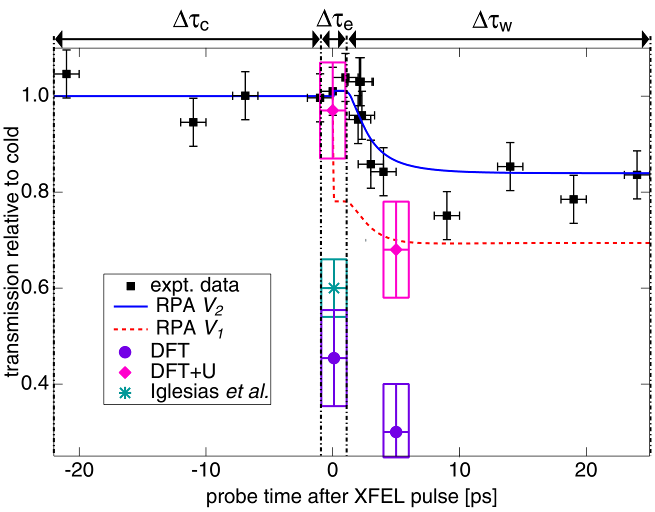

FIG. 7. The same as Fig. 4 with a different vertical scaling and including predictions using DFT calculations. The experimental transmission of zero order (all harmonics) relative to cold of a 600-nm aluminum foil heated by an XFEL pulse (black squares). The time axis is relative to the peak of the XFEL pulse. Calculated transmission values for the electron-ion potential, V_1 (dashed red line) and V_2 (solid blue line), for the average transmission of the probed region are shown. A delay in electron-ion coupling is incorporated into the TTM to give a heating rate in agreement with other studies (detailed in Sec. III). A semianalytic model by Iglesias *et al.* [9] predicting changes due to electron heating is shown in the $\Delta\tau_e$ phase (boxed green star). Standard DFT (solid purple circles) and DFT+U (pink diamonds) are shown with the boxed area representing the uncertainties in temperature and temporal resolution. The three time scales of interest are shown (arrows and dash-dotted lines): $\Delta\tau_c$ is the cold solid foil, $\Delta\tau_e$ is the time scale of electron heating only, and $\Delta\tau_w$ is the time scale of electron-ion coupling.

We restrict our calculations to the three temporal regions of interest shown in Fig. 7 (top arrows). For the DFT calculations the $\Delta\tau_c$ phase corresponds to cold electrons in a crystalline lattice, the $\Delta\tau_e$ phase to $T_e = 6$ eV and a crystalline lattice, and the $\Delta\tau_w$ phase to $T_e = 6$ eV and $T_i = 2$ eV. The standard DFT calculations match reasonably well with the cold solid data in the $\Delta\tau_c$ phase. In the $\Delta\tau_e$ phase, DFT predicts a decrease in transmission which is not observed in the data (boxed solid purple circles in Fig. 7). A further decrease in transmission in the $\Delta\tau_w$ phase is predicted by DFT, resulting in a greatly overestimated decrease in transmission compared to the data in Fig. 7.

To guide our understanding of the changes in the photon absorption process calculated by DFT, the available electronic states and the probability of the optical transition occurring has been calculated. The density of states (DOS), transition probabilities (P_r), electron occupancies, and transitions for 39 eV photons calculated by DFT for the three temporal regions of interest are shown in Fig. 8. The P_r values in Fig. 8 are calculated by taking the average transition matrix element value for a narrow bandwidth of photon energies (between 38 and 39 eV). As these values are discrete, the curve of P_r vs energy is smoothed and divided by 10^{-6} for clarity of representation. The increase in absorption with T_e in a cold solid crystal ($\Delta\tau_e$ phase) is shown to be due to larger values of P_r that are accessible with a higher T_e, as seen in Figs. 8(a) and 8(b). Increasing T_i results in forbidden transitions that exist in the crystal state becoming available, causing an overall smoothing of the DOS and P_r values, resulting in increased absorption [Fig. 8(c)]. From Figs. 8(a) and 8(b), it is clear that accessing the higher-energy states leads to an increase of absorption with T_e, which is not observed experimentally. We investigate changes in the electronic structure using DFT that could account for the experimentally observed behavior.

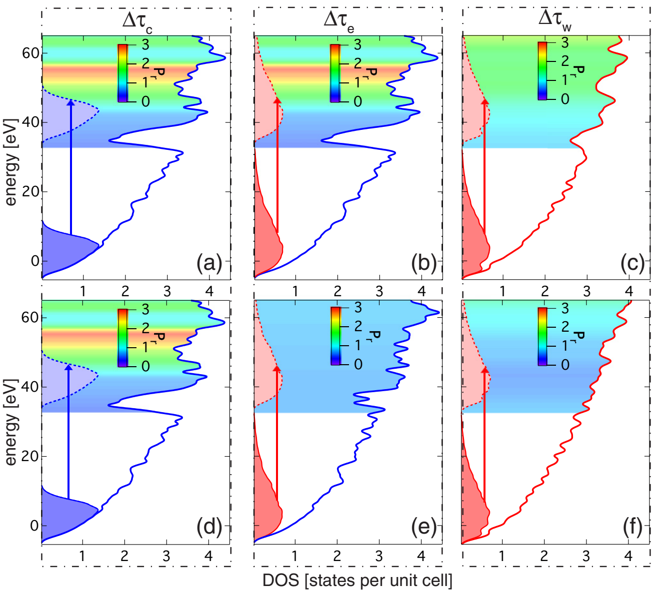

FIG. 8. DFT calculations of the density of states (DOS) (solid lines), electron transitions for 39 eV photons (arrows), and transition probabilities P_r (color-scale shading). The calculations correspond to the three temporal regions of interest ($\Delta\tau_c$, $\Delta\tau_e$, and $\Delta\tau_w$) shown in Fig. 7 (top arrows). The $\Delta\tau_c$ region corresponds to cold electrons in a cold lattice, the $\Delta\tau_e$ phase corresponds to $T_e = 6$ eV in a cold lattice, and $\Delta\tau_w$ corresponds to $T_e = 6$ eV and $T_i = 2$ eV. (a)–(c) Standard DFT calculations corresponding to the DFT points in Fig. 7. (d)–(f) DFT+U calculations corresponding to the DFT+U points in Figs. 5 and 7.

Using standard DFT, a negligible change of the high-energy electronic structure occurs when T_e is increased [as shown in Figs. 8(a) and 8(b)]. However, the optical absorption calculated with standard DFT does not agree with the absorption data (shown in the $\Delta\tau_e$ phase in Figs. 5 and 7). Changes of the electronic structure due to increased T_e have been predicted to occur theoretically [47,54–56], and experiments at temperatures similar to those in this study have indicated changes to the high-energy d-orbital band structure due to electron heating in titanium [57]. As the increased absorption predicted by standard DFT during the $\Delta\tau_e$ phase is not observed experimentally, this implies the high-energy (above 30 eV) electronic structure changes with increased T_e.

We have included an *ad hoc* potential, U, to the higher-energy orbitals in our DFT calculations, which we refer to as DFT+U. For the DFT+U calculations we have used the local spin density approximation (LSDA)+U approach available in the VASP package. The method of Dudarev *et al.* was used to implement an intra-atomic potential in the d orbital of aluminum [58]. The value of the potential used was sufficient to suppress the effect of electron heating on the optical properties, as to agree with the experiment. The value of the potential used was 15 eV. The ion heating was treated in a similar manner as the standard DFT calculations, and the optical properties were averaged over nine separate ion configurations at a temperature of $T_e = 6$ eV and $T_i = 2$ eV. The principle effect of this potential is to smooth the distribution of the higher-energy states in Fig. 8(d) to yield a less structured DOS, as shown in Fig. 8(e). We treat this potential as coming into effect during the $\Delta\tau_e$ phase. Using this potential, the absorption probabilities, P_r, show an overall reduction and a relatively featureless energy dependence [Fig. 8(e)]. This corresponds to minor changes in absorption for increased T_e, and even decreased absorption for the highest photon energy [Fig. 5(a)]. In the $\Delta\tau_w$ phase, an increase in T_i causes an increase in P_r overall [Fig. 8(f)] and matches reasonably well with the data in the $\Delta\tau_w$ phase shown in Figs. 7 and 5. The cold solid absorption values of aluminum calculated using DFT+U are underestimated ($\alpha_c^U = 1.1 \times 10^6\ \mathrm{m}^{-1}$) compared to standard DFT ($\alpha_c^{\mathrm{DFT}} = 2.1 \times 10^6\ \mathrm{m}^{-1}$). This suggests the standard DFT treatment in the cold solid phase can be quite reliable, yet at higher temperatures an intricate dependence of the electronic structure on electronic temperature exists that we have mimicked with the DFT+U approach.

VII. CONCLUSIONS

In conclusion, we have created a highly nonequilibrium solid-density plasma by heating an aluminum foil with a high-intensity XFEL and measured the transient optical properties in the XUV by means of time-resolved HHG transmission spectroscopy. The femtosecond nature of the XFEL and HHG pulses have allowed us to separate the electron and ion temperatures in time and observe the individual effect of each on the optical properties, which was an unresolved question until now. A picosecond-time-scale decrease in transmission was found, consistent with an increase in ion temperature. As the crystal structure decomposes with increasing ion temperature, a range of previously forbidden transitions become available due to symmetry breaking, and photon absorption increases. We show an increase in the electron temperature to have a relatively minor impact on absorption, contrary to several predictions. The (RPA) theory can reproduce the observed behavior using a smoothed potential. However, as the smoothing is chosen to fit the data we cannot infer its correctness, as other elements in the model are also approximate such as the electron dielectric function, which ignores electron-electron interactions. Standard DFT was shown to give reasonable agreement with the cold solid absorption values, yet it overestimates the dependence of absorption on electron temperature. A better agreement with the data for both the $\Delta\tau_e$ and $\Delta\tau_w$ phases is found by adding an *ad hoc* potential to the *d* orbital that smoothes the magnitude of the transition probabilities [Fig. 8(e)]. This suggests a dependence of the electronic structure on the electron temperature which is beyond a mere populating of high-energy electron states. Recent treatments show progress in incorporating electron temperature into DFT in a more self-consistent manner [54,55].

Overall, once the sharp dependence of absorption on electron temperature is mitigated by smoothing the electronic structure, the theoretical and numerical approaches show a much improved fit to the data. This implies that, due to electron heating, a more homogeneous, less structured high-energy electronic structure exists in warm dense aluminum than previously predicted.

ACKNOWLEDGMENTS

Thanks to D. O. Gericke, S. M. Vinko, C. Iglesias, and C. Starrett for valuable interactions regarding this work. Use of the Linac Coherent Light Source (LCLS), SLAC National Accelerator Laboratory, is supported by the U.S. Department of Energy, Office of Science, Office of Basic Energy Sciences under Contract No. DE-AC02-76SF00515. The MEC instrument is supported by the U.S. Department of Energy, Office of Science, Office of Fusion Energy Sciences under Contract No. SF00515. We acknowledge support from Fundação para a Ciência e a Tecnologia (FCT) projects EXPL/FIS-OPT/0889/2012 and PTDC/FIS/112392/2009, COST Action (MP1203), Laserlab-Europe, H2020 EC-GA 654148, and the Swedish Foundation for International Cooperation in Research and Higher Education (STINT). This work was supported by the European Union's Horizon 2020 research and innovation programme (VOXEL H2020-FETOPEN-2014-2015-RIA 665207).

---

[1] F. Graziani, *Frontiers and Challenges in Warm Dense Matter* (Springer, New York, 2014), Vol. 96.

[2] M. C. Dharma-wardana, Computation **4**, 16 (2016).

[3] K. Lejaeghere, G. Bihlmayer, T. Björkman, P. Blaha, S. Blügel, V. Blum, D. Caliste, I. E. Castelli, S. J. Clark, A. Dal Corso *et al.*, Science **351**, aad3000 (2016).

[4] M. S. Murillo, Phys. Rev. Lett. **96**, 165001 (2006).

[5] Y. Ping, D. Hanson, I. Koslow, T. Ogitsu, D. Prendergast, E. Schwegler, G. Collins, and A. Ng, Phys. Rev. Lett. **96**, 255003 (2006).

[6] K. Widmann, T. Ao, M. Foord, D. Price, A. Ellis, P. Springer, and A. Ng, Phys. Rev. Lett. **92**, 125002 (2004).

[7] Z. Chen, B. Holst, S. E. Kirkwood, V. Sametoglu, M. Reid, Y. Y. Tsui, V. Recoules, and A. Ng, Phys. Rev. Lett. **110**, 135001 (2013).

[8] S. X. Hu, L. A. Collins, V. N. Goncharov, T. R. Boehly, R. Epstein, R. L. McCrory, and S. Skupsky, Phys. Rev. E **90**, 033111 (2014).

[9] C. A. Iglesias, High Energy Density Phys. **6**, 311 (2010).

[10] S. M. Vinko, G. Gregori, M. P. Desjarlais, B. Nagler, T. J. Whitcher, R. W. Lee, P. Audebert, and J. S. Wark, High Energy Density Phys. **5**, 124 (2009).

[11] B. Kettle, T. Dzelzainis, S. White, L. Li, B. Dromey, M. Zepf, C. L. S. Lewis, G. Williams, S. Künzel, M. Fajardo, H. Dacasa, P.

Zeitoun, A. Rigby, G. Gregori, C. Spindloe, R. Heathcote, and D. Riley, Phys. Rev. E **94**, 023203 (2016).
[12] A. Levy, P. Audebert, R. Shepherd, J. Dunn, M. Cammarata, O. Ciricosta, F. Deneuville, F. Dorchies, M. Fajardo, C. Fourment *et al.*, Phys. Plasmas **22**, 030703 (2015).
[13] B. Nagler, B. Arnold, G. Bouchard, R. F. Boyce, R. M. Boyce, A. Callen, M. Campell, R. Curiel, E. Galtier, J. Garofoli, E. Granados, J. Hastings, G. Hays, P. Heimann, R. W. Lee, D. Milathianaki, L. Plummer, A. Schropp, A. Wallace, M. Welch, W. White, Z. Xing, J. Yin, J. Young, U. Zastrau, and H. J. Lee, J. Synchrotron Radiat. **22**, 520 (2015).
[14] S. M. Vinko, O. Ciricosta, B. I. Cho, K. Engelhorn, H.-K. Chung, C. R. D. Brown, T. Burian, J. Chalupský, R. W. Falcone, C. Graves, V. Hájková, A. Higginbotham, L. Juha, J. Krzywinski, H. J. Lee, M. Messerschmidt, C. D. Murphy, Y. Ping, A. Scherz, W. Schlotter, S. Toleikis, J. J. Turner, L. Vysin, T. Wang, B. Wu, U. Zastrau, D. Zhu, R. W. Lee, P. A. Heimann, B. Nagler, and J. S. Wark, Nature **482**, 59 (2012).
[15] S. P. Hau-Riege, Phys. Rev. E **87**, 053102 (2013).
[16] A. G. de la Varga, P. Velarde, F. de Gaufridy, D. Portillo, M. Cotelo, A. Barbas, A. González, and P. Zeitoun, High Energy Density Phys. **9**, 542 (2013).
[17] S. Crockett, SESAME 3720, Los Alamos National Laboratory Report No. LA-UR-2004 (2004).
[18] S. I. Anisimov, B. L. Kapeliovich, and T. L. Perel'Man, Zh. Eksp. Teor. Fiz. **66**, 776 (1974) [Sov. Phys. JETP **39**, 375 (1974)].
[19] B. Henke, E. Gullikson, and J. Davis, At. Data Nucl. Data Tables **54**, 181 (1993).
[20] S. Vinko, O. Ciricosta, T. Preston, D. Rackstraw, C. Brown, T. Burian, J. Chalupský, B. Cho, H.-K. Chung, K. Engelhorn *et al.*, Nat. Commun. **6**, 6397 (2015).
[21] Z. Lin, L. Zhigilei, and V. Celli, Phys. Rev. B **77**, 075133 (2008).
[22] B. Rethfeld, A. Kaiser, M. Vicanek, and G. Simon, Appl. Phys. A **69**, S109 (1999).
[23] J. L. Hostetler, A. N. Smith, D. M. Czajkowsky, and P. M. Norris, Appl. Opt. **38**, 3614 (1999).
[24] Z. Li-Dan, S. Fang-Yuan, Z. Jie, and T. Da-Wei, Acta Phys. Sin. **61**, 134402 (2012).
[25] M. W. C. Dharma-wardana and F. Perrot, Phys. Rev. E **63**, 069901 (2001).
[26] M. W. C. Dharma-wardana and F. Perrot, Phys. Rev. E **58**, 3705 (1998).
[27] B. Mueller and B. Rethfeld, Phys. Rev. B **87**, 035139 (2013).
[28] L. Waldecker, R. Bertoni, R. Ernstorfer, and J. Vorberger, Phys. Rev. X **6**, 021003 (2016).
[29] S. Williamson, G. Mourou, and J. C. M. Li, Phys. Rev. Lett. **52**, 2364 (1984).
[30] P.-M. Leguay, A. Lévy, B. Chimier, F. Deneuville, D. Descamps, C. Fourment, C. Goyon, S. Hulin, S. Petit, O. Peyrusse *et al.*, Phys. Rev. Lett. **111**, 245004 (2013).
[31] F. Dorchies, A. Lévy, C. Goyon, P. Combis, D. Descamps, C. Fourment, M. Harmand, S. Hulin, P.-M. Leguay, S. Petit *et al.*, Phys. Rev. Lett. **107**, 245006 (2011).
[32] M. Kandyla, T. Shih, and E. Mazur, Phys. Rev. B **75**, 214107 (2007).
[33] B. Siwick, J. Dwyer, R. Jordan, and R. Miller, J. Appl. Phys. **92**, 1643 (2002).
[34] P. Zhu, J. Chen, R. Li, L. Chen, J. Cao, Z. Sheng, and J. Zhang, Appl. Phys. Lett. **103**, 231914 (2013).
[35] E. Gullikson, P. Denham, S. Mrowka, and J. Underwood, Phys. Rev. B **49**, 16283 (1994).
[36] A. Di Cicco, K. Hatada, E. Giangrisostomi, R. Gunnella, F. Bencivenga, E. Principi, C. Masciovecchio, and A. Filipponi, Phys. Rev. B **90**, 220303 (2014).
[37] A. Ron and N. Tzoar, Phys. Rev. **131**, 12 (1963).
[38] J. J. Hopfield, Phys. Rev. **139**, A419 (1965).
[39] N. R. Arista and W. Brandt, Phys. Rev. A **29**, 1471 (1984).
[40] G. Gregori, A. Ravasio, A. Höll, S. Glenzer, and S. Rose, High Energy Density Phys. **3**, 99 (2007).
[41] L. Fletcher, H. Lee, T. Döppner, E. Galtier, B. Nagler, P. Heimann, C. Fortmann, S. LePape, T. Ma, M. Millot *et al.*, Nat. Photonics **9**, 274 (2015).
[42] T. Dornheim, S. Groth, and M. Bonitz, Contrib. Plasma Phys. **57**, 468 (2017).
[43] C. A. Iglesias, High Energy Density Phys. **7**, 38 (2011).
[44] S. M. Vinko, G. Gregori, and J. S. Wark, High Energy Density Phys. **7**, 40 (2011).
[45] D. O. Gericke, J. Vorberger, K. Wünsch, and G. Gregori, Phys. Rev. E **81**, 065401 (2010).
[46] G. Kresse and J. Hafner, Phys. Rev. B **47**, 558 (1993).
[47] B. Holst, V. Recoules, S. Mazevet, M. Torrent, A. Ng, Z. Chen, S. E. Kirkwood, V. Sametoglu, M. Reid, and Y. Y. Tsui, Phys. Rev. B **90**, 035121 (2014).
[48] S. Mazevet, M. P. Desjarlais, L. A. Collins, J. D. Kress, and N. H. Magee, Phys. Rev. E **71**, 016409 (2005).
[49] G. Kresse and J. Furthmüller, Phys. Rev. B **54**, 11169 (1996).
[50] G. Kresse and J. Furthmüller, Comput. Mater. Sci. **6**, 15 (1996).
[51] J. P. Perdew, K. Burke, and M. Ernzerhof, Phys. Rev. Lett. **77**, 3865 (1996).
[52] H. J. Monkhorst and J. D. Pack, Phys. Rev. B **13**, 5188 (1976).
[53] M. Gajdoš, K. Hummer, G. Kresse, J. Furthmüller, and F. Bechstedt, Phys. Rev. B **73**, 045112 (2006).
[54] V. V. Karasiev, L. Calderín, and S. B. Trickey, Phys. Rev. E **93**, 063207 (2016).
[55] T. Dornheim, S. Groth, T. Sjostrom, F. D. Malone, W. Foulkes, and M. Bonitz, Phys. Rev. Lett. **117**, 156403 (2016).
[56] E. Bévillon, J.-P. Colombier, V. Recoules, and R. Stoian, Phys. Rev. B **89**, 115117 (2014).
[57] E. Principi, E. Giangrisostomi, R. Cucini, F. Bencivenga, A. Battistoni, A. Gessini, R. Mincigrucci, M. Saito, S. D. Fonzo, F. D'Amico, A. D. Cicco, R. Gunnella, A. Filipponi, A. Giglia, S. Nannarone, and C. Masciovecchio, Struct. Dyn. **3**, 023604 (2016).
[58] S. L. Dudarev, G. A. Botton, S. Y. Savrasov, C. J. Humphreys, and A. P. Sutton, Phys. Rev. B **57**, 1505 (1998).